Nonlinear Resonance Characteristics Analysis of DBD Load Based on State Plane Trajectory

Zhaozhe Deng, Xingliang Liu, Qi Qiu, Hefei Jia, Yan Deng, *Senior Member, IEEE*, and Xiangning He, *Fellow, IEEE*

***Abstract*—Dielectric barrier discharge (DBD) loads and driving converters are widely utilized in low-temperature plasma generation, but their resonant tanks have typical nonlinear characteristics with control issues. The state plane trajectory analysis is used in this article to investigate the resonant behavior of a DBD load. The converter's working principle and state plane modeling are first discussed. The impact of a high-ratio step-up transformer with parasitic capacitance is then explored, and the updated trajectory model is examined. The DBD platform is created to verify the suggested model, and the associated experimental data are provided. The results of the experiment demonstrate that the discharge trajectory is a zone with distinct borders. The trajectory equations can be utilized to calculate the load equivalent capacitance, and the difference in the boundary equivalent capacitance represents the discharge intensity. The pattern of resonant frequency variation with discharge power is given. The impact mechanism of discharge phenomena and resonance characteristics is discussed.**

***Index Terms*—Dielectric barrier discharge (DBD), nonlinear load, resonant converter, state plane trajectory.**

I. Introduction

THE resonant switching converter is one of the most popular topologies in current power electronic research. The emergence of the resonant converter was first for the purpose of obtaining ac voltage or current. After years of development, the resonant network is now designed for impedance matching and gain adjustment [1], introducing frequency as an additional power control dimension besides input voltage and duty cycle. Resonant tank design has progressed from two-element resonance to multielement resonance [2], [3], [4], [5], and parasitic parameters can be fully used to improve power density [6], [7].

The frequency response characteristics of common resonant converters may be observed and estimated since their resonant parameters are fixed [8]. However, how to obtain and use the resonant state in a resonant tank with nonlinear parts is a critical topic to address. A typical nonlinear load is the dielectric barrier discharge (DBD) load, which is commonly employed to produce low-temperature plasma or nonthermal equilibrium plasma [9], [10], [11], [12]. DBD adopts the approach of inserting insulating medium between electrodes to retain the gas discharges at the state of corona discharges and filamentous discharges as illustrated in Fig. 1 in order to generate uniform and controllable plasma. Because the resonant converter that drives DBD often treats the load as a component of the resonant tank, it's important to understand DBD's resonant properties.

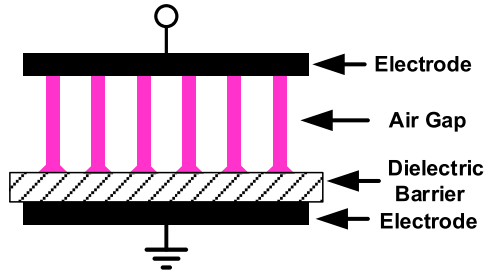

Fig. 1. Basic structure of dielectric barrier discharge (DBD) load.

Due to the reactor structure, the electrical properties of DBD are capacitive basically. Stages of charging and discharging make up the load state. DBD can be equivalent to a capacitor in terms of charging time. As soon as the load begins to discharge, the gas gap voltage is capped, and the load current enters a discrete state with intermittent discharge. The load has a higher capacitance value than its charging equivalent capacitance. Additionally, discharge intensity and load equivalent capacitance are influenced by environmental factors including temperature and humidity [13], [14].

The connection between the applied voltage and working frequency is the main challenge for DBD power control. Discharging power is affected by applied voltage, working frequency, and load equivalent capacitors, according the average power calculation formula [15]. In experiments, the discharge power increases with rising voltage [16]. And the equivalent capacitors grow too, which will undoubtedly modify the resonance frequency and complicate gain control. Therefore, in order to construct a DBD power supply, it is necessary to first measure the load characteristics and establish an accessible electrical model.

The Lissajous figure is universally used to measure the equivalent capacitance of discharge loads [17]. It is about the relationship between the load voltage and the charge flowing through the load. The Lissajous figure of DBD driven by sinusoidal voltage

Manuscript received 1 June 2022; revised 21 August 2022 and 26 October 2022; accepted 28 November 2022. Date of publication 13 December 2022; date of current version 14 February 2023. This work was supported by the Zhejiang Province Public Welfare Technology Application Research Funding under Grant LGF21E070002. Recommended for publication by Associate Editor A. Safaee. *(Corresponding author: Yan Deng.)*

The authors are with the College of Electrical Engineering, Zhejiang University, Hangzhou 310027, China (e-mail: dzz_lyn@zju.edu.cn; liuxingliang@zju.edu.cn; qiuq@zucc.edu.cn; jia123456@zju.edu.cn; dengyan@zju.edu.cn; hxn@zju.edu.cn).

Color versions of one or more figures in this article are available at https://doi.org/10.1109/TPEL.2022.3228786.

Digital Object Identifier 10.1109/TPEL.2022.3228786

is usually a quadrilateral. Between the discharge and charging segments, there are evident turning points. The slopes of different segments represent respective equivalent capacitances and the area enclosed by the figure represents the power consumed by discharges. In some models, the dielectric capacitor is used to define the measured discharge capacitance, whereas the sum of the dielectric capacitor and the gas gap capacitor in series is used to describe the measured charge capacitance [18]. However, because to the change in gas dielectric constant produced by ionization, the dielectric and gas gap capacitances between two stages are not invariable. This defining approach is hard to apply in practice since the values of barrier and gas gap capacitance are difficult to measure directly. In addition, the measured equivalent capacitance value during the discharge phase is a specific value, which makes it impossible to utilize the Lissajous diagram to describe the intermittent pulse phenomenon. It cannot accurately reflect the intensity of the discharge, and a higher discharge power does not necessarily indicate a better discharge outcome. There exists a theory gap between measuring capacitance from Lissajous figure and load behaviors.

A variety of DBD load models are proposed through experiments such as the resistance-capacitance model, controlled current source model, and diode rectifier model [19], [20], [21]. As was already established, DBD has complicated behavior traits, making it challenging to develop a general electrical model. These suggested models make an attempt to provide a partial description of the electrical properties of the discharge phenomenon. In the resistance-capacitance model, the load capacitance is represented by a capacitor and the energy consumption of discharge is represented by a resister without the transient changes. The controlled current source model shows that the discharge power is influenced by the load terminal voltage. The diode rectifier model defines the load capacitance as two series capacitors: 1) dielectric capacitor; and 2) gas gap capacitor. The gas gap capacitor is connected to the voltage source through the diode rectifier bridge. When discharge occurs, the gas gap capacitor is replaced by the voltage source, which shows that the gas gap voltage reaches to and stays at the maintain voltage and load capacitance increase. These common employed models are essentially based on homogenization and steady-state. They lack a description of the discharge process and are unable to capture changes in load characteristics due to discharge.

Since the DBD is one of the resonant elements from the viewpoint of a resonant converter, it could be a feasible research direction to model DBD with resonant converter analysis, which requires a method capable of observing multielement resonance. State plane analysis [22], [23] is a traditional method for analyzing the operation of resonant converters. It picks state variables in the resonant tank, such as inductance current and capacitor voltage, and plots the trajectory on the state plane. The converter state is represented by several trajectories under various resonance circumstances. The resonant converter's functioning can be controlled by planning the trajectory [24]. The state plane analysis was first focused on LC resonant converters, but was gradually expanded to include LLC and LCC converters [25], [26]. Understanding how the resonant element evolves in different resonant states can be simplified by using state plane trajectory for the nonlinear resonant network.

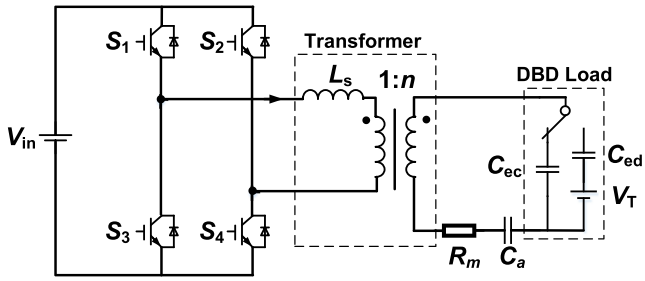

Fig. 2. Typical topology of resonant converter for driving DBD load.

In this article, the state plane trajectory is used to study the nonlinear resonant characteristics of a DBD load at the converter level, which indicates the relationship between the discharge state and the resonance characteristics. The operating principle and state plane analysis of the resonant converter driving the discharge load are introduced in the second section. The resonant characteristics and state plane trajectory with transformer parasitic capacitance are discussed in the third part. Then, the DBD platform is created to verify the suggested model, and the associated experimental data are provided. The results of the experiment demonstrate that the discharge trajectory is a zone with distinct borders. The trajectory equations are used to calculate the load equivalent capacitance, and the difference in the boundary equivalent capacitances can be used to quantitatively represent the discharge intensity. The pattern of resonant frequency variation with discharge power is given, and it is discussed how resonance characteristics and discharge phenomena are related.

II. Operating Principle and State Plane Analysis of Resonant Converter Driving DBD Load

The DBD requires a high working voltage; hence a high ratio step-up transformer can be used to power the discharge load. As shown in Fig. 2, the typical converter topology is adding an inductor, usually an external inductor on the primary side or the leakage inductance of the transformer, in series with the load to form a resonant tank. Because of the two switching resonant states, the resonant converter's working mode is similar to that of an LCC converter. The key distinction is the presence of persistent current spikes induced by discharges.

The DBD load is driven by a converter that operates in discontinuous current mode (DCM). DCM produces a greater peak current at the same power as continuous current mode, making it ideal for low-temperature plasma creation. Furthermore, the DCM working point is lower than the resonance center frequency, allowing the gain to be less affected by frequency.

The DBD load model discussed below no longer distinguishes between dielectric and gas gap capacitance, instead using the measurable quantities of the charging and the discharging equivalent capacitance $C_{\rm ec}$ and $C_{\rm ed}$. Fig. 3 depicts the suggested DBD load model. When discharging, $C_{\rm ec}$ switches to $C_{\rm ed}$ and $C_{\rm ed}$ is connected in series with the maintain voltage source $V_{\rm T}$.

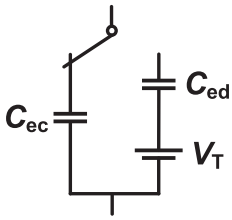

Fig. 3. DBD equivalent capacitance load model.

The time-domain waveform analysis, Lissajous figure, and state plane trajectory will all be studied together in order to fully analyze the DBD load characteristics. Obtaining the amount of reactor charges for the Lissajous figure necessitates the use of a measuring capacitor linked in series at the load end. The charge measurement capacitance, C_a, is shown in Fig. 2. In order to avoid interfering with DBD's functionality, the value of C_a is substantially bigger than the load capacitance. The load current measurement resistance, R_m, is set towards the ground end of the circuit. Because the DBD's working voltage is so high and the load current is so low, the measuring resistor has little effect on the system's efficiency.

The v_g represents the idealized voltage across the gas gap and the absolute value of v_g is clamped at sustaining voltage V_T when the discharge process begins. In experiments, the v_g is difficult to measure directly but the V_T could be obtained by means of Lissajous figure. Here, it is used to show the resonance waveform changes with discharge. The v_{sw} is output voltage of the H-bridge. A whole resonant cycle and a discontinuous interval with zero current are included in each half working cycle of the converter in DCM. Because the operating mode of the negative half cycle is similar to that of the positive half cycle, the study that follows will use the positive half as an example. The input voltage V_{in} and resonance inductance L_s are equivalently transformed to the secondary side as (1) and (2), respectively, to simplify the study of the resonant tank.

$$V_{ins} = \frac{V_{in}}{n} \tag{1}$$

$$L_{ss} = n^2 L_s. \tag{2}$$

The functioning modes of the converter can be separated into Mode 1 and Mode 2 depending on whether the v_g reaches the V_T at the start of resonance. When the v_g does not equal the V_T at the start of the cycle, this is referred to as Mode 1. Fig. 4 shows the waveform of Mode 1 and Fig. 5 shows the resonant equivalent circuit. The four stages of the positive half cycle are as follows.

Stage I **[t_0~t_1]:** All switches are switched OFF before t_0. The load current i_o and the inverter output voltage v_{sw} are zero. The load voltage v_o remains unchanged at -V_e while the value of v_g is V_{Te}. At t_0, S_1 and S_4 are turned ON. C_{ec} is charged as i_o begins to climb. The voltage across the gas gap, v_g, rises to V_T. At the end of this stage, $i_o = I_{br}$ and $v_o = V_{br}$.

Stage II **[t_1~t_2]**: The load begins to discharge at t_1, while the i_o continues to charge the C_{ed}. i_o rapidly declines to zero at t_2 and v_o climbs to the maximum value V_{om} as resonance progresses. The v_g begins to drop, and the discharge comes to a halt.

Stage III **[t_2~t_3]**: At t_2, i_o reverses and starts extracting charge of C_{ec}. The amplitude of i_o increases at first and subsequently falls as a result of resonance, eventually reaching zero at t_3. A complete resonance cycle concludes at this point. The values of v_o and v_g at t_3 are opposite to their values at t_0, according to the half cycle's working symmetry.

Stage IV **[t_3~t_4]**: At t_3, i_o falls to zero, and the resonance cycle comes to an end. Switches and diodes have all been turned

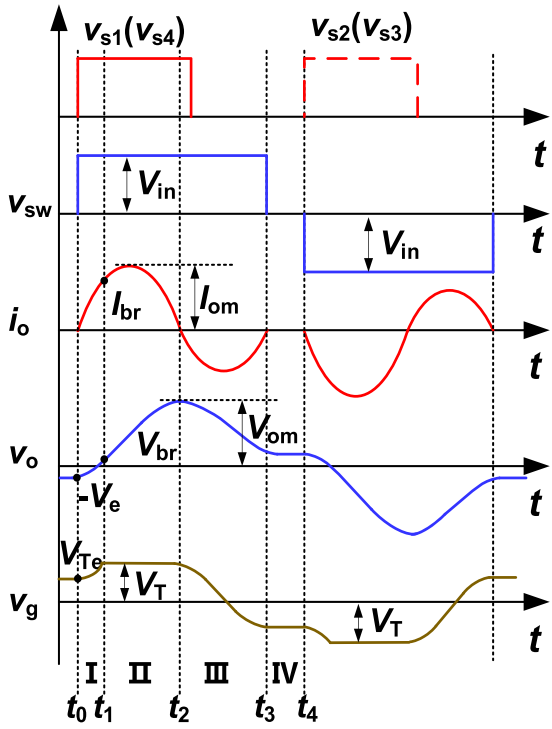

Fig. 4. Waveform of resonant converter in Mode 1.

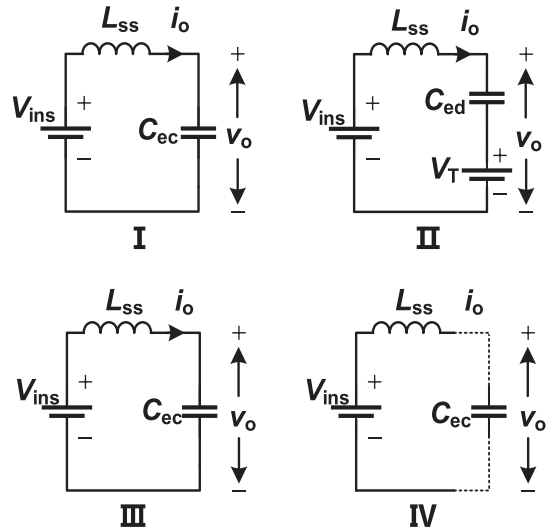

Fig. 5. Equivalent resonant circuit of Mode 1.

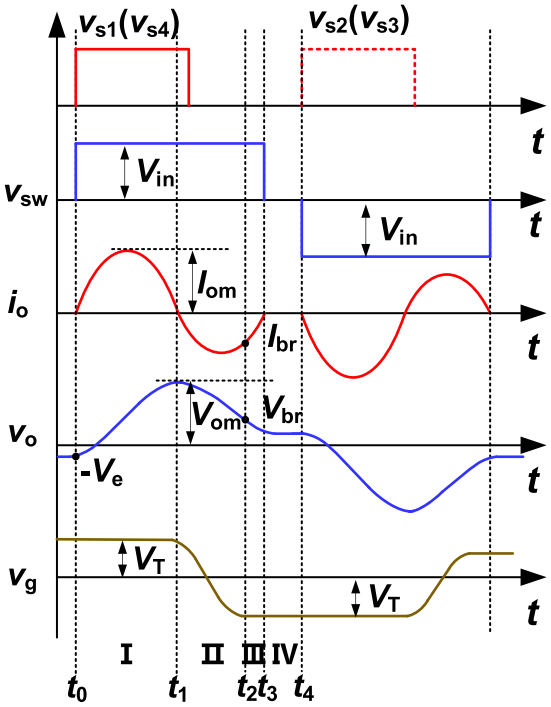

Fig. 6. Waveform of resonant converter in Mode 2.

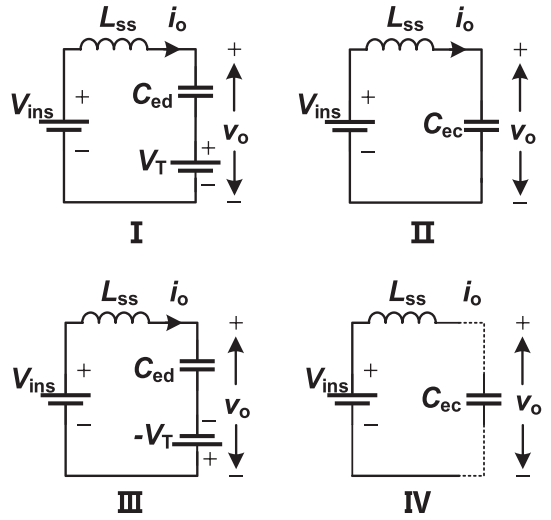

Fig. 7. Equivalent resonant circuit of mode 2.

OFF. Until the second half of the cycle, at t_4, v_o and v_g stay unchanged.

Mode 2 is the situation when the v_g equals V_T at the beginning of the resonant cycle. Figs. 6 and 7 show how the positive half cycle can be separated into four sections.

Stage I **[t_0~t_1]**: In comparison to Mode 1, v_g has reached the clamping voltage V_T at the start of the cycle, whereas v_o = -V_e. S_1 and S_4 are turned ON at t_0, and the load starts to discharge. v_g remains clamped, while i_o rises and begins to charge the capacitor C_{ed}. As the resonance progresses, v_o rises to the peak voltage V_{om} at t_1 and i_o falls to zero, halting the discharge.

Stage II **[t_1~t_2]**: At t_1, the v_g begins to drop and the discharge comes to a halt. The charge of C_{ec} is removed as i_o increases in the opposite direction from zero. v_g goes from positive to negative and continues to drop. At t_2, it reaches -V_T and is clamped once more. The load begins to discharge again.

Stage III **[t_2~t_3]**: When i_o reaches zero at t_3, the discharge stops and the resonance cycle is completed. At t_3, v_o equals V_e according to the half cycle's working symmetry.

Stage IV **[t_3~t_4]**: As in Mode 1, v_o and v_g remain unchanged until the second half of the cycle at t_4.

When compared to Mode 1, Mode 2's discharge time makes up a larger share of the overall cycle. As a result, the discharge application is usually in Mode 2. The following analysis focuses primarily on Mode 2.

The DBD load's state plane trajectory is then derived, ignoring the power loss produced by the devices. The discharge load voltage v_o and load current i_o are chosen as state variables because they are straightforward to obtain in applications. The voltage and current equations between L_{ss} and C_{ed} are presented in (3), (4), and (5), respectively, in the equivalent circuit of stage I in Fig. 7.

$$v_{Lss}(t) = V_{ins} - v_o(t) = V_{ins} - V_T - v_{Ced}(t) \tag{3}$$

$$i_{Lss}(t) = i_o(t) = C_{ed}\frac{dv_{Ced}(t)}{dt} \tag{4}$$

$$v_{Lss}(t) = L_{ss}\frac{di_{Lss}(t)}{dt}. \tag{5}$$

At t_0, the values of i_o and v_o are displayed in (6)

$$\begin{cases} i_o = 0 \\ v_o = -V_e \end{cases}. \tag{6}$$

Under the condition of t_0, the relationship of state variables can be derived as shown in (7).

$$(v_o - V_{ins})^2 + \frac{L_{ss}}{C_{ed}}i_o^2 = (V_e + V_{ins})^2. \tag{7}$$

Similarly, the voltage and current equations of Stage II are as shown in (8), (9), and (10).

$$v_{Lss}(t) = V_{ins} - v_o(t) = V_{ins} - v_{Cec}(t) \tag{8}$$

$$i_{Lss}(t) = i_o(t) = C_{ec}\frac{dv_{Cec}(t)}{dt} \tag{9}$$

$$v_{Lss}(t) = L_{ss}\frac{di_{Lss}(t)}{dt}. \tag{10}$$

At t_2, the values of i_o and v_o are shown in (11)

$$\begin{cases} i_o = 0 \\ v_o = V_{om} \end{cases} \tag{11}$$

where the V_{om} is the output peak voltage.

Under the condition of t_2, the relationship of state variables can be derived as shown in (12).

$$(v_o - V_{ins})^2 + \frac{L_{ss}}{C_{ec}}i_o^2 = (V_{om} - V_{ins})^2. \tag{12}$$

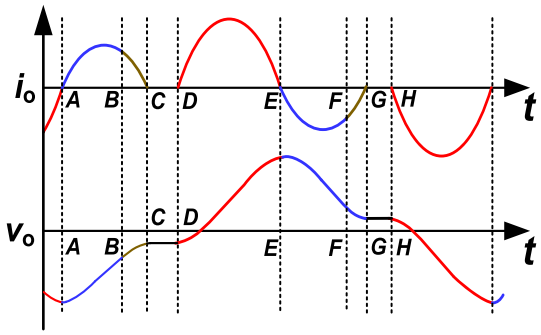

Fig. 8. Waveform of load current i_o and load voltage v_o for mode 2.

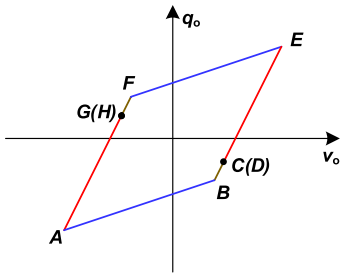

Fig. 9. Lissajous figure for resonant converter with DBD load.

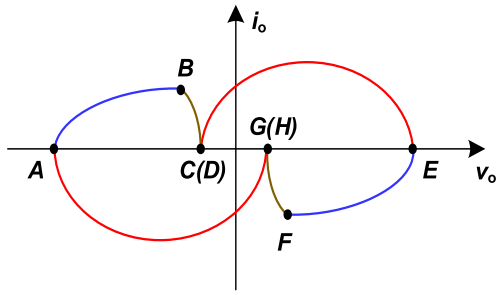

Fig. 10. State plane trajectory of i_o and v_o for Mode 2.

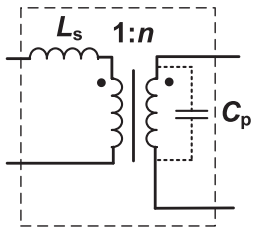

Fig. 11. Transformer model considering parasitic capacitance.

The voltage and current equations of Stage III are as shown in (13), (14), and (15).

$$v_{\mathrm{Lss}}(t) = V_{\mathrm{ins}} - v_{\mathrm{o}}(t) = V_{\mathrm{ins}} + V_{\mathrm{T}} - v_{\mathrm{Ced}}(t) \tag{13}$$

$$i_{\mathrm{Lss}}(t) = i_{\mathrm{o}}(t) = C_{\mathrm{ed}} \frac{dv_{\mathrm{Ced}}(t)}{dt} \tag{14}$$

$$v_{\mathrm{Lss}}(t) = L_{\mathrm{ss}} \frac{di_{\mathrm{Lss}}(t)}{dt}. \tag{15}$$

At t_3, the values of i_o and v_o are shown in (16)

$$\begin{cases} i_{\mathrm{o}} = 0 \\ v_{\mathrm{o}} = V_{\mathrm{e}} \end{cases} \tag{16}$$

where V_e is the load voltage in chopping current phase.

Under the condition of t_3, the relationship of state variables can be derived as shown in the following equation:

$$(V_{\mathrm{ins}} - v_{\mathrm{o}})^2 + \frac{L_{\mathrm{ss}}}{C_{\mathrm{ed}}} i_{\mathrm{o}}^2 = (V_{\mathrm{ins}} - V_{\mathrm{e}})^2. \tag{17}$$

Equations (7), (12), and (17) are the equations for the state plane trajectory throughout the positive half cycle. The trajectory equations are elliptic equations with the horizontal axis as the long axis. In addition to the value of resonant elements, input voltage V_{ins}, initial voltage V_e, and the max output voltage V_{om} are the key parameters that influence the trajectory shape. The equivalent capacitance of the reactor under the same excitation voltage can be estimated using the trajectory equations because the resonant inductance is constant.

Fig. 8 depicts a waveform that varies with i_o and v_o. In Fig. 9, the DBD load is represented by a Lissajous figure. The trajectory of Mode 2 for a whole resonant cycle is illustrated in Fig. 10, with v_o as the horizontal axis and i_o as the vertical axis. The intersection point on the voltage axis has a coordinate expression of in (18). The Lissajous figure develops counterclockwise with time, whereas the trajectory advances clockwise.

$$\begin{aligned} v_{\mathrm{E}} &= -v_{\mathrm{A}} = V_{\mathrm{om}} \\ v_{\mathrm{G(H)}} &= -v_{\mathrm{C(D)}} = V_{\mathrm{e}}. \end{aligned} \tag{18}$$

For positive half cycle, the curve segments DE, EF, and FG correspond to (7), (12), and (17) in Figs. 8–10. The charging periods are AB and EF, and the discharging periods are BC, CE, FG, and GA in a working cycle. The electrodes complete a unidirectional discharge during the AE that does not correspond to the resonant cycle, but rather spans two resonant cycles. Due to a shortage of energy supply during cut-off periods such as CD and GH, discharge is rare. And because the v_o is constant, these segments in Figs. 9 and 10 represent themselves as points. When the current is generated again, however, the discharge begins right away and does not require reaching the initial discharge voltage.

III. Resonance Characteristics Considering Transformer Parasitic Capacitance

The DBD converter's high gain is primarily achieved by a high ratio step-up transformer. Larger interturn parasitic capacitance is produced by more turns and higher insulating requirements. In practice, the magnitude of parasitic capacitance is found to be close to that of load equivalent capacitance. As a result, parasitic capacitance should be taken into account while making resonance analysis.

The parallel parasitic capacitor C_p on the secondary side of the transformer is equivalent to the interturn parasitic capacitance of the winding as Fig. 11. Fig. 12 shows the resonant equivalent circuit after parasitic capacitance is added. In the charging

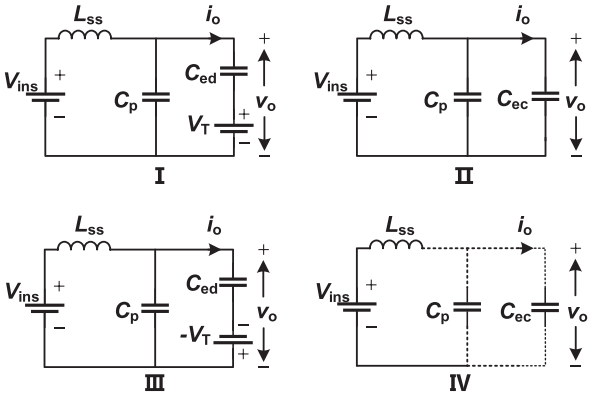

Fig. 12. Equivalent circuit considering parasitic capacitance of transformer.

period, the inductor current i_{Lss} and output voltage v_{o} are as follows in (19) and (20):

$$i_{\mathrm{Lss}} = i_{\mathrm{o}} \frac{C_{\mathrm{ec}} + C_{\mathrm{p}}}{C_{\mathrm{ec}}} \tag{19}$$

$$v_{\mathrm{o}} = v_{\mathrm{Cp}} = v_{\mathrm{Cec}}. \tag{20}$$

In the discharging period, the inductor current i_{Lss} and output voltage v_{o} are as follows in (21) and (22):

$$i_{\mathrm{Lss}} = i_{\mathrm{o}} \frac{C_{\mathrm{ed}} + C_{\mathrm{p}}}{C_{\mathrm{ed}}} \tag{21}$$

$$v_{\mathrm{o}} = v_{\mathrm{Cp}} = v_{\mathrm{Ced}} + V_{\mathrm{T}}. \tag{22}$$

The parasitic capacitance shares a portion of the resonant current since it is connected in parallel with the load. The observed output current i_{o} shifts from total resonant current to branch resonant current, which should be transformed throughout trajectory equations in the solution process. Substitute (19)∼(22) into voltage and current equations between L_{ss} and C_{ec} in Section II and the equations for the state plane trajectory with parasitic capacitance can be derived as (23), (24), and (25)

$$(V_{\mathrm{o}} - V_{\mathrm{ins}})^2 + \frac{L_{\mathrm{ss}}(C_{\mathrm{ed}} + C_{\mathrm{p}})}{C_{\mathrm{ed}}^2} i_{\mathrm{o}}^2 = (V_{\mathrm{e}} + V_{\mathrm{ins}})^2 \tag{23}$$

$$(V_{\mathrm{o}} - V_{\mathrm{ins}})^2 + \frac{L_{\mathrm{ss}}(C_{\mathrm{ec}} + C_{\mathrm{p}})}{C_{\mathrm{ec}}^2} i_{\mathrm{o}}^2 = (V_{\mathrm{om}} - V_{\mathrm{ins}})^2 \tag{24}$$

$$(V_{\mathrm{ins}} - V_{\mathrm{o}})^2 + \frac{L_{\mathrm{ss}}(C_{\mathrm{ed}} + C_{\mathrm{p}})}{C_{\mathrm{ed}}^2} i_{\mathrm{o}}^2 = (V_{\mathrm{ins}} - V_{\mathrm{e}})^2. \tag{25}$$

The state plane trajectory can be depicted using the preceding equations as Fig. 13, and the matching time domain waveform can be seen as Fig. 14. Compared with Figs. 8 and 10, when the charging region is moved to the discharge area, there is a sudden jump in current on the load. This is due to the fact that C_{ec} is less than C_{ed}, and the i_{o} will be growing at the time of changeover. For the ideal resonance process, the current will remain continuous. But the parasitic capacitance affected resonance no longer exhibits a smooth transition and the branch current is redistributed after switching. When the discharge area is changed to the charging area, the current is zero and

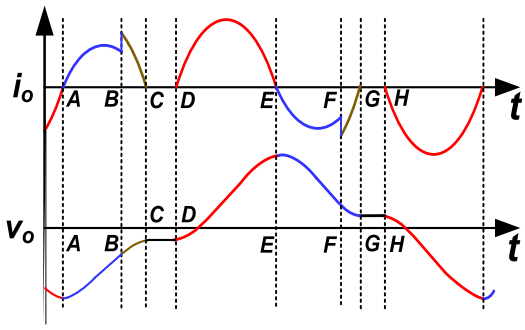

Fig. 13. Waveform of load current i_{o} and load voltage v_{o} with the parasitic capacitance.

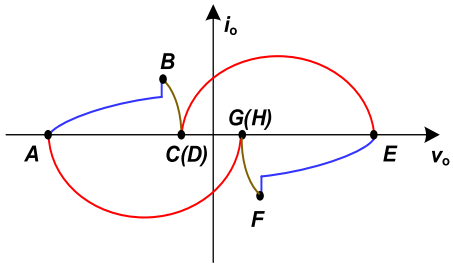

Fig. 14. State plane trajectory of i_{o} and v_{o} with the parasitic capacitance.

TABLE I
CONVERTER SPECIFICATIONS

Parameter	Value
Transformer parasitic capacitance	0.12 nF
Transformer turns ratio	1:30
Resonant inductance (L_{s})	13.07 μH
Switching frequency (f_{sw})	30 kHz
Measuring resistor (R_{M})	20 Ω
Measuring capacitor (C_{M})	66 nF

will not change. The state plane trajectory will also reflect the phenomenon in load current.

In a traditional converter, a quick shift in current will reduce the stability of the system. The discharge process in a DBD driving converter, on the other hand, is always accompanied by a constant pulse current, and current fluctuation only occurs on the high voltage side of the transformer, causing no harm to semiconductor devices. Otherwise, the Lissajous figure's measuring charges only include the DBD load portion, so parasitic capacitance's influence is not apparent.

IV. EXPERIMENTAL RESULTS

The physical phenomena and nonlinear behaviors of gas discharge are not captured by circuit analysis, hence the model must be verified through experiments. As a result, a DBD platform is constructed, and the parameter design, which includes the power supply and the DBD reactor, is explained in this section.

The converter topology is shown in Fig. 2. Table I lists the circuit's parameters. The input voltage is 220 V from the

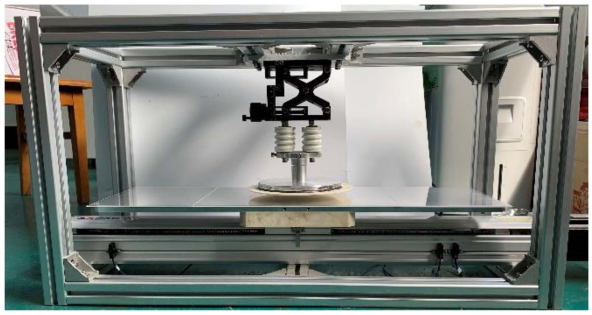

Fig. 15. DBD reactor includes electrodes and quartz medium.

Fig. 16. Photo of DBD phenomenon during work.

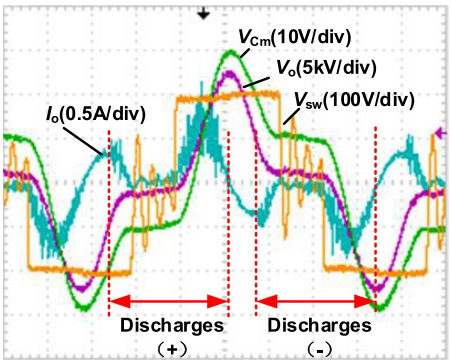

Fig. 17. Experiment waveforms of load voltage $V_{\rm o}$, load current $I_{\rm o}$, bridge voltage $V_{\rm sw}$, and measuring capacitor voltage $V_{\rm Cm}$ ($V_{\rm e}$ = 900 V, $V_{\rm om}$ = 12.6 kV).

power grid and is regulated using a buck converter at the front stage. To ensure that the converter operates in DCM, the power switchers' operating frequency is adjusted to 30 kHz, which is less than the resonance center frequency. Resonant inductance is the sum of external series inductance and transformer leakage inductance. The transformer winding parasitic capacitance at the high voltage side is measured by a sinusoidal signal source.

As shown in Fig. 15, the discharge electrode is asymmetric. A disk-shaped high voltage electrode with a diameter of 140 mm is used. A rectangular electrode with a length of 700 mm and a width of 200 mm serves as the grounding electrode. With a thickness of 2 mm, the insulating quartz medium covers the grounding electrode. The gas gap is fixed at 1 mm. The load voltage $v_{\rm o}$ is measured by high voltage probe P6015A. The load current $i_{\rm o}$ is measured by a 20-Ω resistor ($R_{\rm M}$) connected in series with the ground electrode. The charge of Lissajous figure is obtained by using a 66 nF series capacitor ($C_{\rm M}$). The discharge picture is shown in Fig. 16.

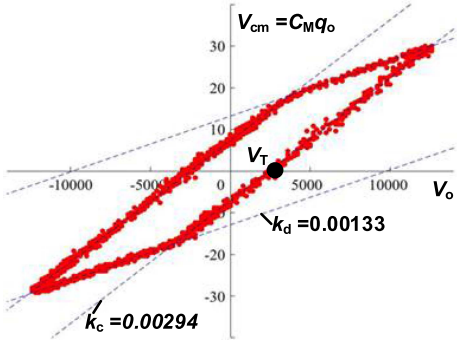

Fig. 18. Lissajous figure drawn from the experiment data ($V_{\rm T}$ = 2.412 kV).

In Fig. 17, $V_{\rm sw}$ of the H-bridge, the load current $i_{\rm o}$, the load voltage $v_{\rm o}$ and $V_{\rm Cm}$ of the measure capacitor are shown. The input voltage $V_{\rm in}$ is 195 V and the max output voltage $V_{\rm om}$ is 12.6 kV. It should be noted that while the $v_{\rm o}$ remains constant in theoretical analysis during the cutoff time, it falls in experiment due to circuit resistance and natural charge loss in the gas gap. During the cutoff period of DCM, obvious ringing phenomenon can be observed in the waveform of $V_{\rm sw}$. This is because the resonant inductor continues to resonate with the capacitance in the circuit, such as the parasitic capacitance of the switches, which does not affect the normal operation of the circuit. The waveform of $i_{\rm o}$ in the discharging portions displays a continuous and densely organized pulse current, while its envelope retains the shape of resonant current. It is generally accepted that the bigger the number and peak magnitude of pulse currents, the greater the discharge intensity. Because of the asymmetric construction, the discharge of the positive half cycle is substantially more intense than the negative half. However, this change in discharge intensity is difficult to quantify.

The Lissajous figure is drawn as a scatter diagram in Fig. 18 based on $V_{\rm o}$ and $V_{\rm Cm}$, with the shape of a parallelogram in this experiment. The calculated power based on the figure's area is 485 W. The figure's horizontal axis crossover point is $V_{\rm T}$, and the value is 2.412 kV. The discharging equivalent capacitance $C_{\rm ed}$ is represented by the slope of the discharge interval $k_{\rm d}$, whereas the charging equivalent capacitance $C_{\rm ec}$ is represented by the slope of the charge interval $k_{\rm c}$. By calculating the slope, it can be concluded that $C_{\rm ed}$ = 0.194 nF and $C_{\rm ec}$ = 0.087 nF.

The state plane trajectory of $v_{\rm o}$ and $i_{\rm o}$ is shown in Fig. 19. The "Lissajous trajectory" is a trajectory curve based on the equivalent capacitance calculated from the Lissajous figure. The Lissajous trajectory roughly matches the actual trajectory curve throughout the charging period, as can be observed. The difference from the theoretical waveform mainly lies in the discharge period. The discharge trajectory is now spread across a region with upper and lower bounds, rather than being a curve. The Lissajous trajectory is almost in the middle of the discharge zone. The trajectory equations can also be used to compute the boundary conditions. The equivalent capacitance of the upper boundary $C_{\rm ub}$ in the positive discharging area is 0.300 nF, while the lower boundary capacitance $C_{\rm lb}$ is 0.088nF, with the average

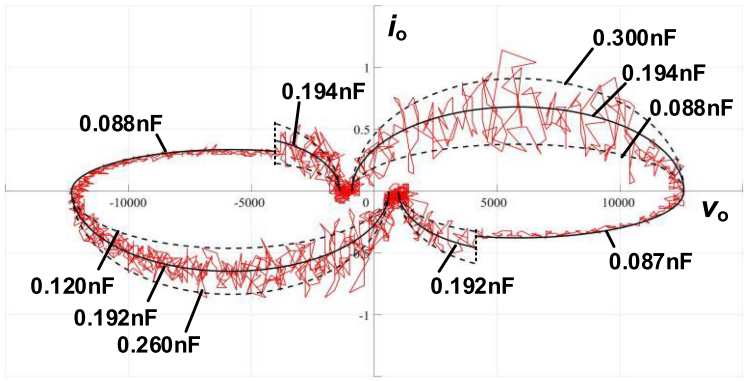

Fig. 19. State plane trajectory of i_o and v_o when $V_{in} = 195$ V and $V_{om} = 12.6$ kV.

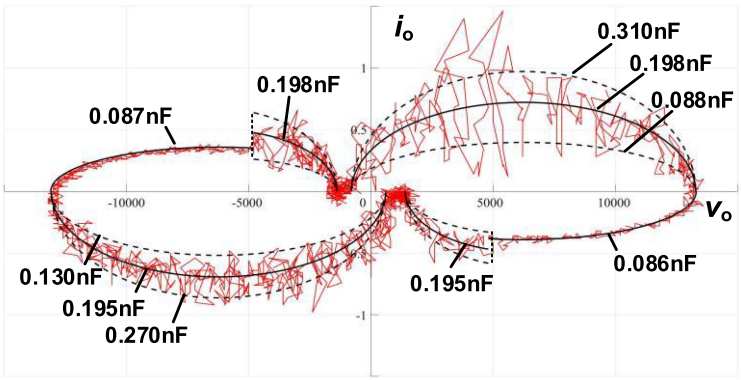

Fig. 20. State plane trajectory of i_o and v_o when $V_{in} = 208$ V and $V_{om} = 13.5$ kV.

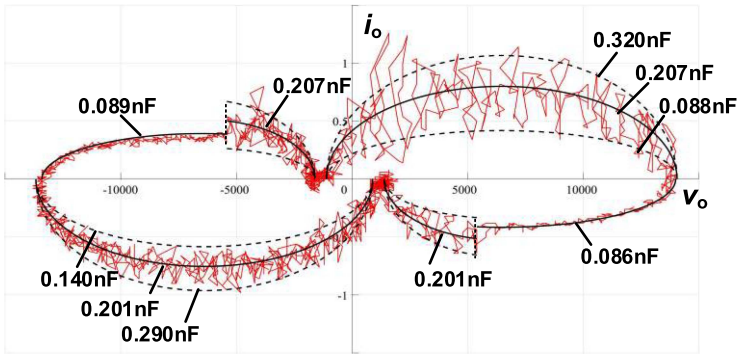

Fig. 21. State plane trajectory of i_o and v_o when $V_{in} = 216$ V and $V_{om} = 14.0$ kV.

being roughly identical to the C_L observed by the Lissajous figure. Furthermore, the positive discharge trajectory has a larger coverage area than the negative discharge trajectory. It shows that the positive discharge is more intense than the negative discharge.

The trajectory diagrams in Figs. 20 and 21 are for output voltages of 13.5 kV and 14.0 kV, respectively. With the increase of voltage, the area covered by the envelope of the discharge trajectory increases and has a similar shape. This proves that the discharge becomes more intense. The equivalent capacitance calculated from the Lissajous trajectory and the upper discharge barrier increases as well, indicating a trend in load characteristics as external voltage varies. Similar to the situation in Fig. 19, the Lissajous trajectories of the discharge area are located in the middle of the upper and lower boundaries too. This shows that the Lissajous capacitance is about equal to the average of the upper and lower boundary capacitance.

Figs. 22–24 provide data for the high voltage side's peak voltage, Lissajous capacitance, boundary capacitance, and resonance center frequency with discharge powers ranging from 300 to 650 W. The C_{ec} and C_{lb} of the positive and negative discharge areas remain virtually unchanged as the voltage and discharge power increase, whereas the upper boundary capacitance C_{ub} and Lissajous capacitance C_L steadily rise. In addition, it should

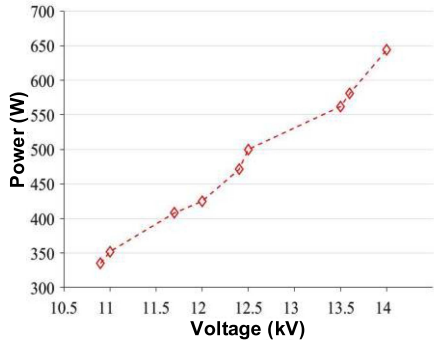

Fig. 22. Discharge power for various peak voltage.

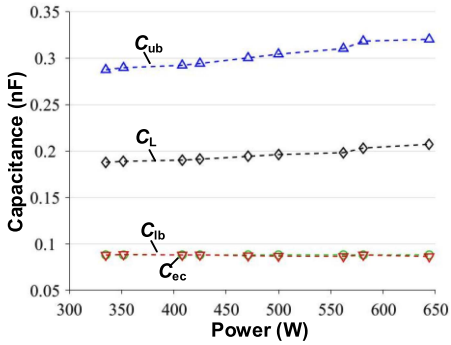

Fig. 23. Equivalent capacitances for various discharge power in the positive discharge period.

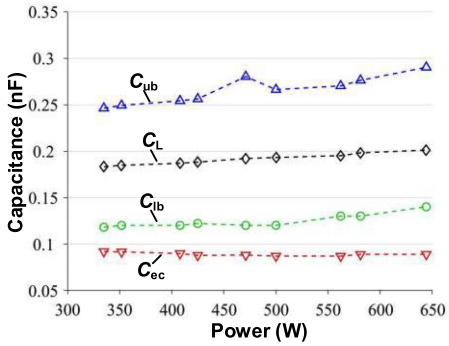

Fig. 24. Equivalent capacitances for various discharge power in the negative discharge period.

be noted that the positive discharge's C_{lb} is lower than that of the negative discharge.

The center frequency f_{d} of the resonance network composed of discharge equivalent capacitance, parasitic capacitance, and inductance is shown in Fig. 25. It is clear that raising the voltage and discharge power will cause the resonance center frequency of the discharge to fall. When the working frequency is lower than f_{d}, raising the discharge power causes the resonance gain to spontaneously grow. A higher discharge power will result in a lower central resonance frequency and resonance gain when the working frequency is higher than f_{d}. The above behavior is more pronounced where the working frequency is near the f_{d}. In the opposite case, it little affects the gain. Therefore, when formulating the control strategy for the DBD driving power

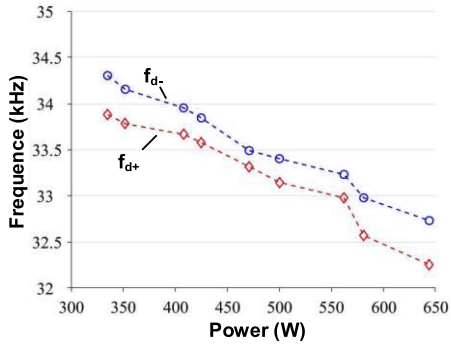

Fig. 25. Resonance center frequencies for various discharge power in the discharge period. ($f_{\mathrm{d}+}$ is the center frequency in the positive discharge period and $f_{\mathrm{d}-}$ is the center frequency in the negative discharge.).

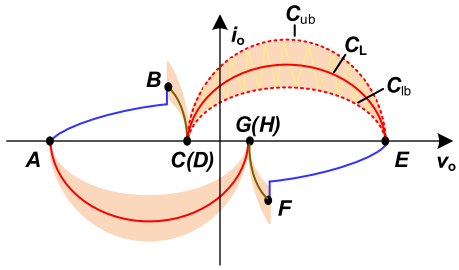

Fig. 26. Trajectory characteristics of DBD with boundary equivalent capacitance.

supply, it is important that the voltage and frequency must be adjusted synchronously to obtain the optimal transmission power.

V. Discussion

The trajectory and resonant features of DBD can be summarized using experimental data in Fig. 26 as follows.

1) During the charging period, the resonant properties of the DBD load are similar to those of the *LC* resonance. Its state plane trajectory is a curve that roughly corresponds to the Lissajous trajectory.
2) During the discharge period, the state plane trajectory of DBD load covers a certain area with apparent envelopes. The trajectory oscillates between the two borders. In the centre of the discharge region lies the Lissajous trajectory.

In comparison to the Lissajous figure, the state plane trajectory analysis naturally and thoroughly displays the change process of the resonant characteristics with the converter and components. The trajectory equations can also be used to determine the equivalent capacitance measured by the Lissajous figure. The Lissajous figure, on the other hand, can better compute discharge consumption power and discharge maintain voltage V_{T}.

When the load characteristics of DBD are integrated with the gas discharge theory, the load characteristics of DBD may be further explained. When discharge begins, the gas gap contains a number of discharging channels that are randomly dispersed. These discharge channels have a brief life span and occur on a regular basis. Discharging channels can be thought of as short-circuit paths, resulting in a reduction in the average distance

between electrodes. According to the capacitance characteristic formula, the shorter the distance, the greater the capacitance. When discharge channels exist, the upper border of the discharge trajectory denotes the maximum equivalent capacitance. When the discharge channels disappear, the bottom border of the discharge trajectory reflects the minimal equivalent capacitance. As a result, the discharge trajectory shows a circular motion between the two boundaries. The switch of the load equivalent capacitance can be characterized as the movement of the track.

Furthermore, as the discharge intensity increases, the number and volume of discharge channels increases, raising the load equivalent capacitance. The experimental results reveal that as the supply voltage rises, the upper boundary trajectory capacitance rises as well. The lower border capacitance reveals varied circumstances depending on the discharge polarity. The value of the lower border capacitance is nearly equivalent to the value of the charging capacitance during positive discharge. Negative discharge, on the other hand, has a lower boundary capacitance that is clearly greater than the charging capacitance. The asymmetric electrode structure is to account for this phenomenon. Close to the negative electrode is where the dielectric is inserted. During the intermittent phase of positive discharge, most of the energy is dissipated in the gas gap, whereas during the intermittent period of negative discharge, some of the energy is stored on the medium's surface. Actually in Fig. 24, it has been observed that the C_{lb} increases slightly, which is caused by the increase the medium surface charge with more intense discharge. In a double dielectric barrier discharge, this distinction may not exist.

The change in discharge degree can be represented by a state plane trajectory and equivalent capacitance. As a result, the discharge intensity may be quantified using the capacitance difference ΔC_{eq} between the upper and lower boundary capacitances C_{ub} and C_{lb} as (26). The more intense the discharge, the higher the value of ΔC_{eq}. Moreover, observing the distribution of discharge trajectory in a single cycle, which can show discharge uniformity, is convenient. Positive discharge, e.g., has a sparser and more irregular trajectory than negative discharge in Figs. 18–20.

$$\Delta C_{\mathrm{eq}} = C_{\mathrm{ub}} - C_{\mathrm{lb}}. \tag{26}$$

The equivalent capacitance C_{L} produced from the Lissajous figure is also identical to the average value of C_{ub} and C_{lb} as a result of the experiment in (27). This is because the Lissajous figure is about the charge–voltage relationship and charge is the integral of current. The discharge current's fluctuation features in the trajectory tend to average out after integration, so the Lissajous trace lies in the middle of the discharge area. Without adding an additional capacitor to construct the Lissajous figure, the Lissajous capacitance can be calculated using trajectory analysis.

$$C_{\mathrm{L}} = \frac{C_{\mathrm{ub}} + C_{\mathrm{lb}}}{2}. \tag{27}$$

The situation depicted in the experiment is a fairly uniform discharge. The discharge continues to deviate from the trajectory model in several regions. The intensity of discharge fluctuates to some extent due to factors such as electrode surface uniformity and gas composition distribution, which is outside the model's predictive capacity.

VI. Conclusion

In this article, the state plane trajectory approach is used to study the resonant properties of DBD in DCM. The experimental data show that the DBD discharge period trajectory does not follow the normal resonant converter curve trajectory but rather appears to cover the region with distinct boundaries. The trajectory oscillates between the boundaries, which embodies the properties of nonlinear resonance. This research suggests that the discharge intensity increases with the rising difference in boundary capacitance and it can be used to quantitatively define the discharge intensity, which make up for the drawbacks of conventional measuring methods. The rise in upper boundary capacitance and average equivalent capacitance of the discharge area, as well as the decrease in the calculated resonant center frequency, are also mentioned as effects of increasing voltage. Some suggestions on the control strategy of driving power supply are given. Finally, the physical explanation of the above phenomena based on the theory of gas discharge is discussed.

References

[1] P. K. Jain, "Resonant power conversion: Insights from a lifetime of experience," *IEEE J. Emerg. Sel. Topics Power Electron.*, vol. 9, no. 6, pp. 6561–6576, Dec. 2021.

[2] D. Huang, F. C. Lee, and D. Fu, "Classification and selection methodology for multi-element resonant converters," in *Proc. IEEE 26th Annu. Appl. Power Electron. Conf. Expo.*, 2011, pp. 558–565.

[3] J. Koscelnik, M. Frivaldsky, M. Prazenica, and R. Mazgut, "A review of multi-elements resonant converters topologies," in *Proc. IEEE ELEKTRO*, 2014, pp. 312–317.

[4] X. Tan and X. Ruan, "Equivalence relations of resonant tanks: A new perspective for selection and design of resonant converters," *IEEE Trans. Ind. Electron.*, vol. 63, no. 4, pp. 2111–2123, Apr. 2016.

[5] L. Yang, Y. Wang, C. Wang, W. Li, and M. Chen, "A topology morphing multi-element resonant converter with wide voltage gain range," in *Proc. IEEE Appl. Power Electron. Conf. Expo.*, 2018, pp. 803–807.

[6] J. Liu, T. Guo, L. Chang, and X. He, "Effects of the parasitic capacitance on characteristics of series resonant converters," *Proc. CSEE*, vol. 32, no. 15, pp. 16–23, 2012.

[7] R. Beiranvand, B. Rashidian, M. R. Zolghadri, and S. M. Hossein Alavi, "A design procedure for optimizing the LLC resonant converter as a wide output range voltage source," *IEEE Trans. Power Electron.*, vol. 27, no. 8, pp. 3749–3763, Aug. 2012.

[8] R. L. Steigerwald, "A comparison of half-bridge resonant converter topologies," *IEEE Trans. Power Electron.*, vol. 3, no. 2, pp. 174–182, Apr. 1988.

[9] C. Charles, "Grand challenges in low-temperature plasma physics," *Front. Phys.*, vol. 2, p. 39, Jun. 2014.

[10] B. Eliasson and U. Kogelschatz, "Modeling and applications of silent discharge plasmas," *IEEE Trans. Plasma Sci.*, vol. 19, no. 2, pp. 309–323, Apr. 1991, doi: 10.1109/27.106829.

[11] U. Kogelschatz, "Dielectric-barrier discharges: Their history, discharge physics, and industrial applications," *Plasma Chem. Plasma Process.*, vol. 23, no. 1, pp. 1–46, Mar. 2003.

[12] H. E. Wagner, R. Brandenburg, K. V. Kozlov, A. Sonnenfeld, P. Michel, and J. F. Behnke, "The barrier discharge: Basic properties and applications to surface treatment," *Vacuum*, vol. 71, no. 3, pp. 417–436, May 2003.

[13] W. J. Park et al., "Effect of dielectric barrier discharge on surface modification characteristics of polyimide film," *Surf. Coatings Technol.*, vol. 201, no. 9–11, pp. 5017–5020, 2007.

[14] A. Flores-Fuentes et al., "Electrical model of an atmospheric pressure dielectric barrier discharge cell," *IEEE Trans. Plasma Sci.*, vol. 37, no. 1, pp. 128–134, Jan. 2009.

[15] S. Wang, Y. Konishi, M. Ishitobi, S. Shirakawa, and M. Nakaoka, "Current-source type parallel inductor-compensated load resonant inverter with PDM control scheme for efficient ozonizer," in *Proc. IEEE Int. Power Electron. Conf.*, 1998, pp. 103–110.
[16] M. Amjad, Z. Salam, M. Facta, and K. Ishaque, "A simple and effective method to estimate the model parameters of dielectric barrier discharge ozone chamber," *IEEE Trans. Instrum. Meas.*, vol. 61, no. 6, pp. 1676–1683, Jun. 2012.
[17] X. Bonnin, J. Brandelero, N. Videau, H. Piquet, and T. Meynard, "A high voltage high frequency resonant inverter for supplying DBD devices with short discharge current pulses," *IEEE Trans. Power Electron.*, vol. 29, no. 8, pp. 4261–4269, Aug. 2014.
[18] H. Sugimura, B. Saha, H. Omori, H.-W. Lee, and M. Nakaoka, "Single reverse blocking switch type pulse density modulation controlled ZVS inverter with boost transformer for dielectric barrier discharge lamp dimmer," in *Proc. IEEE CES 5th Int. Power Electron. Motion Control Conf.*, 2006, pp. 1–5.
[19] H. Fujita and H. Akagi, "Control and performance of a pulse-density-modulated series-resonant inverter for corona discharge processes," *IEEE Trans. Ind. Appl.*, vol. 35, no. 3, pp. 621–627, May/Jun. 1999.
[20] A. Eid, K. Takashima, and A. Mizuno, "Experimental and simulation investigations of DBD plasma reactor at normal environmental conditions," *IEEE Trans. Ind. Appl.*, vol. 50, no. 6, pp. 4221–4227, Nov./Dec. 2014.
[21] O. Koudriavtsev, S. Wang, Y. Konishi, and M. Nakaoka, "A novel pulse-density-modulated high-frequency inverter for silent-discharge-type ozonizer," *IEEE Trans. Ind. Appl.*, vol. 38, no. 2, pp. 369–378, Mar./Apr. 2002.
[22] R. Oruganti and F. C. Lee, "Resonant power processors, part I—State plane analysis," *IEEE Trans. Ind. Appl.*, vol. IA-21, no. 6, pp. 1453–1460, Nov. 1985.
[23] C. Lee and K. Siri, "Analysis and design of series resonant converter by state-plane diagram," *IEEE Trans. Aerosp. Electron. Syst.*, vol. AES-22, no. 6, pp. 757–763, Nov. 1986.
[24] L. Wu, J. Zhao, H. Lin, X. Sun, and G. Chen, "State trajectory control of startup for LCC resonant converters with capacitive output filter," *IEEE J. Emerg. Sel. Topics Power Electron.*, vol. 9, no. 2, pp. 2317–2327, Apr. 2021.
[25] J. Zhao et al., "Fast and accurate control strategy for LCC resonant converters based on simplified state trajectory and two-point solution method," *IEEE Trans. Power Electron.*, vol. 37, no. 5, pp. 5309–5319, May 2022.
[26] W. Feng, F. C. Lee, and P. Mattavelli, "Simplified optimal trajectory control (SOTC) for LLC resonant converters," *IEEE Trans. Power Electron.*, vol. 28, no. 5, pp. 2415–2426, May 2013.

Zhaozhe Deng received the B.S. degree in electrical engineering from Xidian University, Xi'an, China, in 2016 and the M.S. degree in electrical engineering from Shandong University, Jinan, China, in 2019. He is currently working toward the D.Eng. degree in electrical engineering the College of Electrical Engineering, Zhejiang University, Hangzhou, China.

His research interests include multilevel high-voltage converters and resonant converters in the applications of low-temperature plasma.

Xingliang Liu received the B.S. degree in electrical engineering from the Department of Electrical Engineering, Shandong University, Jinan, China, in 2012, and the Ph.D. degree in electrical engineering from Zhejiang University, Hangzhou, China, in 2022.

From May 2014 to February 2015, he was a Research Intern with GE Global Research Center, Shanghai, China. His research interests include reliability and control of resonant power conversion, and high-voltage converters in the industrial applications of low-temperature plasma.

Qi Qiu received the B.S. and M.S. degrees in mechanical and electronic engineering from the College of Mechanical Engineering and Applied Electronics Technology, Beijing University of Technology, Beijing, China, in 2005 and 2009, respectively. He is currently working toward the Ph.D. degree in electrical engineering with the College of Electrical Engineering, Zhejiang University, Hangzhou, China.

From July 2009 to July 2015, he was a Lecturer with the School of Engineering, Zhejiang University City College. His research interests include industrial application of non-thermal plasma for the removal of waste gas.

Hefei Jia received the B.S. degree in electrical engineering from the College of Electrical and Electronic Engineering, Zhengzhou University (ZZU), Zhengzhou, China, in 2014, and the M.S. degree in electrical engineering from Xi'an Jiaotong University (XJTU), Xi'an, China, in 2019. He is currently working toward the Ph.D. degree in electrical engineering with Zhejiang University, Hangzhou, China.

His current research interests include control algorithms and diagnosis of modular multilevel converters.

Yan Deng (Senior Member, IEEE) received the B.E.E. degree in electrical engineering from the Department of Electrical Engineering, Zhejiang University, Hangzhou, China, in 1994, and the Ph.D. degree in power electronics and electric drives from the College of Electrical Engineering, Zhejiang University, Hangzhou, China, in 2000.

Since 2000, he has been a Faculty Member with Zhejiang University, teaching and conducting research on power electronics. He is currently a Professor with Zhejiang University. His research interests include topologies and control for switch-mode power conversion.

Xiangning He (Fellow, IEEE) received the B.Sc. and M.Sc. degrees in electrical engineering from the Nanjing University of Aeronautical and Astronautical, Nanjing, China, in 1982 and 1985, respectively, and the Ph.D. degree in electrical engineering from Zhejiang University, Hangzhou, China, in 1989.

From 1985 to 1986, he was an Assistant Engineer with the 608 Institute of Aeronautical Industrial General Company, Zhuzhou, China. From 1989 to 1991, he was a Lecturer with Zhejiang University. In 1991, he obtained a Fellowship from the Royal Society of U.K., and conducted research with the Department of Computing and Electrical Engineering, Heriot-Watt University, Edinburgh, U.K., as a Postdoctoral Research Fellow for two years. In 1994, he joined Zhejiang University as an Associate Professor. Since 1996, he has been a Full Professor with the College of Electrical Engineering, Zhejiang University. He was the Director of the Power Electronics Research Institute, the Head of the Department of Applied Electronics, the Vice Dean of the College of Electrical Engineering, and he is currently the Director of the National Specialty Laboratory for Power Electronics, Zhejiang University. His research interests include power electronics and their industrial applications.

Dr. He was appointed as IEEE Distinguished Lecturer by the IEEE Power Electronics Society during 2011–2015. He is a Fellow of the Institution of Engineering and Technology (formerly IEE), U.K.